

Obscured star formation at $z = 0.84$ with HiZELS*: the relationship between star formation rate and $H\alpha$ or ultra-violet dust extinction

Timothy Garn¹†, David Sobral¹, Philip N. Best¹, James E. Geach², Ian Smail², Michele Cirasuolo³, Gavin B. Dalton^{4,5}, James S. Dunlop¹, Ross J. McLure¹, Duncan Farrah⁶

¹*SUPA, Institute for Astronomy, Royal Observatory Edinburgh, Blackford Hill, Edinburgh, EH9 3HJ, UK*

²*Institute for Computational Cosmology, Durham University, South Road, Durham, DH1 3LE, UK*

³*Astronomy Technology Centre, Royal Observatory Edinburgh, Blackford Hill, Edinburgh, EH9 3HJ, UK*

⁴*Astrophysics, Department of Physics, Keble Road, Oxford, OX1 3RH, UK*

⁵*Space Science and Technology, Rutherford Appleton Laboratory, HSIC, Didcot, OX11 0QX, UK*

⁶*Astronomy Centre, Department of Physics and Astronomy, University of Sussex, Brighton, BN1 9QJ, UK*

3 November 2018

ABSTRACT

We compare $H\alpha$, ultraviolet (UV) and infrared (IR) indicators of star formation rate (SFR) for a well-defined sample of $z = 0.84$ emission-line galaxies from the High- z Emission Line Survey (HiZELS). Using emission-line, optical, IR, radio and X-ray diagnostics, we estimate that 5 – 11 per cent of $H\alpha$ emitters at this redshift are active galactic nuclei. We detect 35 per cent of the $H\alpha$ emitters individually at $24\ \mu\text{m}$, and stack the locations of star-forming emitters on deep $24\text{-}\mu\text{m}$ *Spitzer Space Telescope* images in order to calculate the typical SFRs of our $H\alpha$ -emitting galaxies. These are compared to the observed $H\alpha$ line fluxes in order to estimate the extinction at $z = 0.84$, and we find a significant increase in dust extinction for galaxies with higher SFRs. We demonstrate that the relationship between SFR and extinction found in the local Universe is also suitable for our high-redshift galaxies, and attribute the overall increase in the typical dust extinction for $z = 0.84$ galaxies to an increase in the average SFR, rather than to a change in dust properties at higher redshift. We calculate the UV extinction, and find a similar dependence on SFR to the $H\alpha$ results, but no evidence for a $2175\ \text{\AA}$ UV bump in the dust attenuation law for high-redshift star-forming galaxies. By comparing $H\alpha$ and UV indicators, we calculate the conversion between the dust attenuation of nebular and stellar radiation, γ , and show that $\gamma = 0.50 \pm 0.14$. The extinction / SFR relationship is shown to be applicable to galaxies with a range of morphologies and bulge-to-disk ratios, to both merging and non-merging galaxies, and to galaxies within high- and low-density environments, implying that it is a fundamental property of star-forming regions. In order to allow future studies to easily correct for a SFR-dependent amount of dust extinction, we present an equation to predict the extinction of a galaxy, based solely upon its observed $H\alpha$ luminosity, and use this to recalculate the $H\alpha$ luminosity function and star formation rate density at $z = 0.84$.

Key words: infrared: galaxies, galaxies: evolution, galaxies: high-redshift, galaxies: ISM

1 INTRODUCTION

There are many methods of estimating the global star formation rate (SFR) of a galaxy, from measurements of the ultra-violet (UV) emission coming directly from visible young massive stars, to the bolometric infrared (IR) luminosity resulting from dust-

reprocessed stellar emission (see Kennicutt 1998, for a review of various star formation indicators). All SFR indicators suffer from different biases and uncertainties, and while SFRs estimated in different ways in the local Universe are now in general agreement, there is much greater scatter in the results at $z \sim 1$ (see, e.g. Hopkins & Beacom 2006).

Locally one of the best measures of the current rate of star formation within a galaxy comes from observations of the $H\alpha$ transition of atomic hydrogen. The luminosity of this recombination line scales directly with the rate of ionising flux from young, massive stars and gives an excellent indication of the presence of ongoing

* Based on observations obtained with the Wide Field CAMera (WFCAM) on the United Kingdom Infrared Telescope (UKIRT), as part of the ‘High- z Emission Line Survey’ (HiZELS) campaign project.

† E-mail: tsg@roe.ac.uk

star formation. However, its usefulness as a quantitative SFR indicator is reduced by the effect of dust obscuration; observed $H\alpha$ line fluxes need to be corrected for extinction before the intrinsic $H\alpha$ luminosity can be recovered, and the SFR calculated.

The initial method used to estimate $H\alpha$ extinction came from a comparison of thermal radio emission, which is unaffected by dust attenuation, and the observed $H\alpha + [\text{N II}]$ line emission within local galaxies (Kennicutt 1983). Disentangling thermal and non-thermal radio emission is non-trivial (see, e.g. Condon 1992, for more details), as thermal radio emission is only a small fraction of the total radio luminosity of a galaxy ($\lesssim 10$ per cent at 1.4 GHz; Condon & Yin 1990), and so this method is not often used in practise.

A much more common method to estimate extinction in individual galaxies comes from the ‘Balmer decrement’, comparing the observed value of the $H\alpha/H\beta$ line flux ratio to the intrinsic value when no dust is present. This allows a calculation of the reddening between the wavelengths of the $H\alpha$ and $H\beta$ lines and, with a choice of dust attenuation model (e.g. Calzetti et al. 2000), permits an estimate of the attenuation at a given wavelength (see e.g. Moustakas, Kennicutt & Tremonti 2006). However, this technique requires sensitive spectroscopy to obtain the line flux ratio with a good signal-to-noise ratio (SNR), which is time-consuming for large samples of galaxies at moderate redshifts. It is therefore more usual for studies with limited available photometry to simply assume that a single extinction can be applied to all galaxies. The canonical amount of $H\alpha$ extinction for a typical galaxy is usually taken to be $A_{H\alpha} \sim 1$ mag (e.g. Kennicutt 1983; Bell & Kennicutt 2001; Pascual et al. 2001; Charlot et al. 2002; Fujita et al. 2003; Brinchmann et al. 2004; Ly et al. 2007; Geach et al. 2008; Sobral et al. 2009a), based upon measurements of extinction in the local Universe.

At higher redshift, the appropriate $H\alpha$ extinction for a typical galaxy is not well determined. Significant numbers of extremely dusty galaxies have been discovered at high redshift (e.g. Chapman et al. 2005), and the large dust content implies a greater $H\alpha$ attenuation. The global rate of star formation increases out to $z \sim 1$ (e.g. Hopkins & Beacom 2006), and galaxies with higher SFR are thought to undergo greater extinction (Hopkins et al. 2001; Sullivan et al. 2001; Berta et al. 2003), also implying that the typical $H\alpha$ attenuation will be greater at $z \sim 1$ than in the local Universe. Villar et al. (2008) have estimated that the typical $H\alpha$ extinction of galaxies within their $z = 0.84$ sample is ~ 1.5 mag.

The total IR luminosity of a galaxy is a bolometric measurement of the thermal emission from dust grains, which have been heated by the UV and optical radiation produced by young massive stars (e.g. Kennicutt 1998). For star-forming galaxies with a reasonable dust content, this emission gives a direct measurement of the total stellar power output. However, since longer wavelength IR emission will more closely trace the cool dust component within a galaxy, which predominantly results from heating by an old stellar component rather than from recent star formation, it could be argued that mid-IR emission might be a better SFR indicator than the bolometric IR luminosity (e.g. Dopita et al. 2002).

Rieke et al. (2009) have demonstrated that the flux density measured in the *Spitzer Space Telescope* 24- μm band can be used as a good proxy for SFR for galaxies at $z = 0$, and, after applying suitable corrections, has a comparable accuracy to estimating SFRs from the extinction-corrected Pa α luminosity or total IR luminosity for normal galaxies in the redshift range $0 < z < 2$. Observations at 24 μm have the additional advantage over longer wavelength IR observations in that they are more sensitive (thus allow-

ing fainter, more distant galaxies to be studied), and have a higher resolution (~ 6 arcsec, making it relatively straightforward to identify counterparts at other wavelengths; the 70- and 160- μm *Spitzer* bands only have resolutions of ~ 20 and ~ 40 arcsec respectively). These disadvantages will be overcome to some extent with *Herschel*, which should be able to make sensitive ~ 6 arcsec resolution images of galaxies at 70 μm , close to the peak in luminosity for the spectral energy distribution (SED) of a typical galaxy at $z \sim 0$.

In this work, we compare $H\alpha$, UV and IR SFR indicators in order to estimate the extinction for a well-defined sample of galaxies at $z = 0.84$, using data from the High- z Emission Line Survey (HiZELS; Geach et al. 2008; Sobral et al. 2009a,b). HiZELS is a panoramic extragalactic survey making use of the wide area coverage of the Wide Field Camera on the 3.8-m UK Infrared Telescope (UKIRT). Narrow-band observations of the Cosmological Evolution Survey field (COSMOS; Scoville et al. 2007a), and the Subaru-XMM-UKIDSS Ultra Deep Survey field (UDS; Lawrence et al. 2007) have been taken in the *J*, *H* and *K* bands in order to target $H\alpha$ emitters at $z = 0.84$, $z = 1.47$ and $z = 2.23$ respectively; this paper concentrates on the properties of the $z = 0.84$ $H\alpha$ sample, the creation of which is described in full in Sobral et al. (2009a).

In Section 2 we present details of the HiZELS sample selection, and the available multi-wavelength data in the COSMOS and UDS fields. In Section 3 we describe various methods which we use to identify active galactic nuclei (AGN) contaminants, and quantify the fraction of $H\alpha$ -emitting sources which may be AGN at $z = 0.84$. We describe our method for stacking galaxies and measuring typical 24- μm flux densities in Section 4, and convert our stacking results into SFRs in order to estimate the $H\alpha$ extinction that is required to make this indicator agree with the IR-based SFRs. In Section 5 we discuss our results, investigate the effects that a variable extinction has on the $H\alpha$ luminosity function at $z = 0.84$, and present a method for correcting observed $H\alpha$ luminosities for a SFR-dependent amount of extinction. Section 6 reports our conclusions.

Throughout this work we assume a concordance cosmology of $\Omega_M = 0.3$, $\Omega_\Lambda = 0.7$ and $H_0 = 70 \text{ km s}^{-1} \text{ Mpc}^{-1}$. All magnitudes are given in the AB system (Oke & Gunn 1983).

2 HIZELS SAMPLE SELECTION

We give a brief overview of the HiZELS sample selection procedure below; full details can be found in Sobral et al. (2009a). Emission-line candidates were selected on the basis of a flux excess in a narrow *J*-band filter centred on $\lambda = 1.211 \mu\text{m}$, compared with deep *J*-band continuum observations. Spurious sources (mainly artifacts due to bright stars) were cleaned from the sample, and spectroscopic and photometric redshifts were used to identify and remove sources found to be a different line emitter at another redshift (such as $H\beta$ or $[\text{O III}]$ at $z \sim 1.5$).

The $H\alpha$ line flux for each source was calculated from the measured flux densities in the narrow and broad-band filters, as described in Sobral et al. (2009a). No aperture corrections were applied to the $H\alpha$ flux, since the correction factor is expected to be minimal. Contamination from the nearby $[\text{N I}]$ lines at 6548 and 6583 \AA was corrected for, using the relationship between the flux ratio $F_{[\text{N I}]} / F_{H\alpha}$ and the total measured equivalent width $\text{EW}(H\alpha + [\text{N I}])$ from Villar et al. (2008), with the median correction factor being 25 per cent.

The final HiZELS $H\alpha$ sample consisted of 477 $H\alpha$ -emitting

sources in COSMOS and 266 in UDS, over a total area of 1.30 deg^2 , at a redshift of $z = 0.845 \pm 0.021$, down to an average observed 3σ $\text{H}\alpha$ line flux limit of $8 \times 10^{-17} \text{ erg s}^{-1} \text{ cm}^{-2}$.

2.1 The HiZELS COSMOS sample

Ground-based observations of the COSMOS field have been made at a variety of UV, optical and near-IR wavelengths, and Capak et al. (2007) have produced a point-spread function (PSF)-matched catalogue for all sources with I -band magnitude < 25 . This catalogue contains data from observations with the Canada France Hawaii Telescope (CFHT; u^* and i^* bands¹), the Sloan Digital Sky Survey (SDSS $ugriz$ bands; Abazajian et al. 2004) and the Subaru telescope ($B_J, V_J, g^+, r^+, i^+, z^+$ and NB816 bands), along with K_s -band data taken from a combination of observations from the Cerro Tololo International Observatory and the Kitt Peak National Observatory. Further details on the catalogue construction can be found in Capak et al. (2007). All of the COSMOS $\text{H}\alpha$ emitters have counterparts in this PSF-matched catalogue.

Mid-IR and far-IR observations of COSMOS have been taken as part of the *Spitzer*-COSMOS survey (S-COSMOS; Sanders et al. 2007; Le Floch et al. 2009). 464 of the $\text{H}\alpha$ emitters (97 per cent) have a counterpart in Infrared Array Camera (IRAC) observations of the field, in at least one of the 3.6-, 4.5-, 5.8- and 8- μm bands. Several of our AGN classification diagnostics rely upon the availability of IRAC information (see Section 3); for this reason, we reject the 13 sources without IRAC detections from our study. To determine whether there is any potential bias from this exclusion, we repeated all tests in Section 4 while retaining these sources – no significant differences were seen in our results.

There have been several *Spitzer* 24- μm surveys of the COSMOS field, and we have used the most recent of these, the Multi-band Imaging Photometer for *Spitzer* (MIPS) Cycle 3 observations², in this work. The public source catalogue is cut at a flux density limit of 0.15 mJy ($\sim 7\sigma$), and 158 $\text{H}\alpha$ emitters had a counterpart in this catalogue, where we consider that an $\text{H}\alpha$ emitter has a counterpart if the positions of the 24- μm and optical source centres are within 3 arcsec. We estimate the percentage of $\text{H}\alpha$ emitters which may have an incorrect 24- μm association by shifting their positions by +10 arcmin in declination and recalculating the number of matches – nine spurious associations were made, which implies an overall percentage of $\text{H}\alpha$ emitters with individual 24- μm counterparts of 34 ± 2 per cent. Throughout this work, all matching percentages have been corrected for false matches in this way.

1.4-GHz radio observations of the COSMOS field have been taken with the Very Large Array (VLA; Schinnerer et al. 2004, 2007; Bondi et al. 2008). The $\text{H}\alpha$ emitters are located within the VLA-COSMOS Deep Project area, which has a typical noise level of between 10 and 40 $\mu\text{Jy beam}^{-1}$, and 21 $\text{H}\alpha$ emitters (4.5 ± 0.9 per cent) have 1.4-GHz counterparts within 3 arcsec. The full HiZELS region of the COSMOS field has been observed with *XMM-Newton* (Cappelluti et al. 2009), and the majority of the region has been observed with *Chandra* (Elvis et al. 2009) – 7 (1.5 ± 0.4 per cent) and 8 (1.7 ± 0.2 per cent) $\text{H}\alpha$ emitters have X-ray counterparts within 3 arcsec respectively, with 5 $\text{H}\alpha$ emitters having counterparts from both surveys.

2.2 The HiZELS UDS sample

The UDS field is the location of a very deep UKIRT near-IR survey in the J, H and K bands (Warren et al. 2007). There is additional deep imaging data available from Subaru (B_J, V_J, r^+, i^+, z^+ bands; Furusawa et al. 2008), and u^* -band data from CFHT.

A deep *Spitzer* legacy survey of the UDS field has been carried out with both IRAC and MIPS (SpUDS; P.I. J. Dunlop). Catalogue production is still ongoing, but mosaics of the SpUDS survey have been delivered to the community³. We use a preliminary version of the IRAC catalogue (M. Cirasuolo et al., in preparation), which excludes regions of the UDS image near to bright stars, image artifacts or the mosaic edges – 234 of the $\text{H}\alpha$ emitters are in regions covered by this catalogue. We exclude a further four sources from our analysis because they are either outside or on the edge of the SpUDS 24- μm image, leaving 230 sources, all of which had optical / IR counterparts. Photometry for all bands was measured within a 1.8 arcsec diameter aperture, equivalent to roughly $2\times$ the size of point spread function for the optical and near-IR images.

We make use of the finely sampled 24- μm SpUDS image of the field (1.245 arcsec/pixel). This image has asteroid streaks visible; we inspected the locations of the $\text{H}\alpha$ emitters to confirm that these imaging artifacts would not affect our analysis. 84 of the UDS emitters (37 ± 3 per cent) had counterparts in the preliminary 24- μm source catalogue, which we have cut at 0.1 mJy ($\sim 6\sigma$), using the same matching criteria as for the COSMOS field.

Radio observations of the UDS field have been taken at 1.4 GHz (Simpson et al. 2006), and three of the $\text{H}\alpha$ emitters (1.3 ± 0.4 per cent) have 1.4-GHz counterparts above 100 μJy . *XMM-Newton* observations of the field have been taken as part of the larger Subaru/*XMM* Deep Survey (Ueda et al. 2008), and four of the $\text{H}\alpha$ emitters (1.7 ± 0.4 per cent) have X-ray counterparts.

3 IDENTIFICATION OF AGN CONTAMINANTS

The HiZELS selection process identifies $\text{H}\alpha$ emitters within the redshift range of $z = 0.845 \pm 0.021$. While most of these sources are likely to be powered by star formation, there will be some objects where AGN activity dominates the energetics – SFRs estimated from these sources will not be accurate, and these contaminants need removing from the sample. We adopt a number of methods for classifying sources as ‘possible’ or ‘likely’ AGN, with the number of sources satisfying each of the criteria listed in Table 1.

3.1 SED template fitting

The matched optical and IR photometry available for each $\text{H}\alpha$ emitter was described in Section 2. This photometry was blue-shifted to the source rest-frame and fitted to a series of template SEDs (shown in Fig. 1; Dale et al. 2001; Polletta et al. 2007), using a standard χ^2 minimization procedure. Only the data with the highest SNR was used out of multiple observations at similar wavelengths, such as the SDSS u and CFHT u^* bands. The SEDs consisted of star-forming galaxies (spiral, elliptical and starburst templates), Seyferts, and AGN templates (Type-1, Type-2, and two composite starburst/AGN templates). Sources which were best fitted by an AGN SED were classified as ‘possible’ AGN candidates – we do not classify sources as ‘likely’ AGN through this automatic fitting procedure, as the range of SED templates is limited to a few

¹ Throughout this work we retain the notation of Capak et al. (2007) to differentiate between observations in different filter systems.

² available via <http://www.ifa.hawaii.edu/~ilbert/S-Cosmos/>

³ available via <http://ssc.spitzer.caltech.edu/legacy/spudshistory.html>

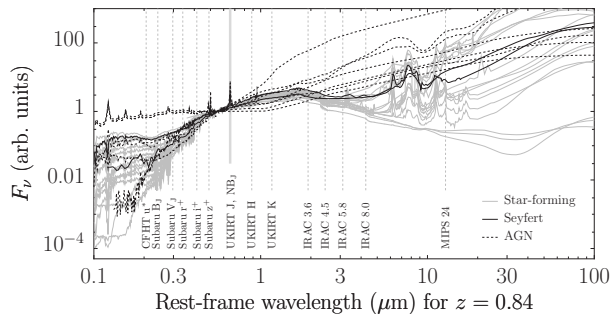


Figure 1. The template SEDs used to fit the H α emitters, taken from Dale et al. (2001) and Polletta et al. (2007) and shown in the galaxy rest-frame, arbitrarily normalised to a flux density of 1 at 5500 Å. The vertical dashed lines indicate the effective wavelengths of the available photometry for sources at $z = 0.84$, with the narrow/broad-band J selection shown by the thicker grey line. Note the difference in AGN and star-forming galaxy mid-IR SED shapes.

per source type, and may not fully represent the HiZELS population. Fig. 1 shows that while there is a large amount of photometric information available for the H α emitters, there is very little difference between the colours of the Seyfert and Starburst templates where photometry is available – for this reason, sources that were best-fitted by Seyfert templates were excluded from this automatic classification.

The SEDs of all sources were inspected to confirm the results of the automatic fitting, and to identify any further objects which appeared to be potential AGN, but had not been classified as such. Four further sources were manually classified as possible AGN; these typically had a similar shape to the AGN templates but had an offset in the IR to optical flux densities, and for this reason were not automatically classified as AGN.

3.2 Colour-colour diagnostics

We use a number of colour-colour diagnostics to identify further AGN contaminants. For each, we classified sources located within the selection region as ‘likely’ AGN, while those located within the region, but with errors on their flux densities sufficiently large enough to potentially place them outside the region, were classified as ‘possible’ AGN.

We used the mid-IR selection criteria of Stern et al. (2005) to define a region of IRAC colour-colour space that principally contains AGN, which is shown on Fig. 2(a), along with the positions of the H α emitters with detections in all four IRAC bands. The objects which have been flagged as potential AGN contaminants lie well away from the remainder of the population.

Stern et al. (2005) warn that their criteria may preferentially omit AGN at $z \simeq 0.8$, where the difference in mid-IR colours between star-forming galaxies and AGN becomes less distinct. Fig. 1 shows that the composite black-body spectrum of galaxies powered by star formation peaks at around 1.6 μm , and falls at longer wavelengths. Warm dust located near to an AGN increases the luminosity of the mid-IR continuum, and Fig. 1 indicates that the AGN templates continue to rise with wavelength throughout the mid-IR. For this reason we add a further AGN classification for sources that are outside of the Stern et al. (2005) region, but have a rising SED between the 3.6- and 4.5- μm bands (which probe rest-frame 1.9- to 2.4- μm dust emission), which is also shown on Fig. 2(a).

It is difficult to conclusively discriminate between Seyfert and

Table 1. The number of H α emitters classified as ‘possible’ or ‘likely’ AGN under each of the criteria described in Section 3. Several sources fulfilled more than one criterion, so the total number of sources classified as AGN is less than the sum of the individual classifications. Sources with two or more ‘possible’ classifications were considered to be ‘likely’ AGN. Values in parentheses represent the number of sources which were only flagged as AGN under a single criterion.

Method	Type	COSMOS	UDS	Total
Automatic SED fit	Possible	17 (10)	20 (10)	37 (20)
Manual SED fit	Possible	4 (4)	0 (0)	4 (4)
Stern wedge	Possible	3 (2)	17 (8)	20 (10)
Stern wedge	Likely	7 (0)	2 (0)	9 (0)
[3.6] – [4.5] colour	Possible	1 (1)	2 (1)	3 (2)
[3.6] – [4.5] colour	Likely	4 (3)	0 (0)	4 (3)
Mid- to far-IR slope	Possible	3 (3)	2 (0)	5 (3)
Mid- to far-IR slope	Likely	9 (1)	5 (0)	14 (1)
X-ray counterpart	Likely	10 (3)	4 (0)	14 (3)
Low value of q_{24}	Likely	1 (0)	3 (3)	4 (3)
Emission-line ratio	Likely	≥ 3 (2) ^a	-	≥ 3 (2) ^a
H α emitters		464	230	694
Possible AGN		20	19	39
Likely AGN		22	15	37
AGN contamination		5 – 9%	7 – 15%	5 – 11%
Sources retained for analysis		422	196	618

^a This value is a lower limit, as only 26 COSMOS sources (6 per cent) had spectroscopy with sufficient SNR for this method.

starburst galaxies, given the available photometry – the optical SED shape of the two source types can be very similar, with the main difference being the increased amount of 24- μm emission for starbursts. We use the shape of the mid-IR to far-IR SED to define a region $R(5.8, 8, 24)$ that contains Seyferts, from inspection of Fig. 1;

$$R(5.8, 8, 24) \equiv ([8] - [24] < 2 \text{ and } [5.8] - [8] > -0.1). \quad (1)$$

The first criterion distinguishes between Seyferts and starbursts, and the second criterion prevents more quiescent source types such as spirals and elliptical galaxies from being flagged. Fig. 2(b) shows the selection region for these criteria, which also includes the other AGN SEDs shown on Fig. 1.

3.3 X-ray detections

The COSMOS field has been observed with both *XMM-Newton* and *Chandra* (Ueda et al. 2008; Elvis et al. 2009), and the UDS field has been observed with *XMM-Newton* (Cappelluti et al. 2009). The catalogue flux limits are equivalent to luminosity limits in the 2–10 keV energy band of $3 \times 10^{43} \text{ erg s}^{-1}$, $2.5 \times 10^{42} \text{ erg s}^{-1}$ and $1 \times 10^{43} \text{ erg s}^{-1}$ respectively, for sources at $z = 0.845$. Purely star-forming galaxies can emit X-rays, but locally are not observed to have luminosities exceeding $L_{0.5-8 \text{ keV}} \approx 3 \times 10^{42} \text{ erg s}^{-1}$ (Bauer et al. 2004) – all of the H α emitters with an X-ray detection have luminosities significantly above this value, and are classified as ‘likely’ AGN.

3.4 Radio-loud sources

We use the IR / radio correlation (e.g. Appleton et al. 2004) to distinguish between radio emission resulting from AGN and star-formation activity, for the H α emitters with radio counterparts.

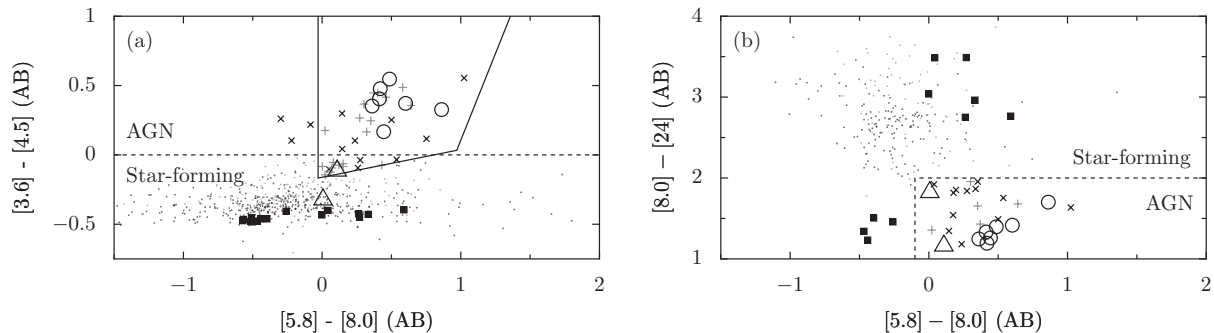


Figure 2. Infrared colour-colour plots showing the HiZELS H α emitters (COSMOS galaxies with black dots, UDS galaxies with grey dots; AGN candidates with black diagonal crosses and grey upright crosses respectively). AGN selection regions are indicated by the lines: (a) the Stern et al. (2005) criteria is shown with the solid line, and the additional 3.6- to 4.5- μ m criterion is indicated by the dashed line; (b) the region $R(5.8, 8, 24)$ is indicated by the dashed line. The colours of the SEDs shown on Fig. 1 are also plotted for reference, separated into star-forming galaxies (solid black squares), Seyferts (open triangles) and AGN (open circles).

22/24 of these had catalogued 24- μ m counterparts – visual inspection of the MIPS images confirmed the lack of a counterpart for the remaining two sources, and we place a conservative upper limit of 0.1 mJy on the 24- μ m flux density of these sources.

The logarithmic ratio of 24- μ m and 610-MHz flux densities is 0.55 ± 0.4 for star-forming galaxies at $z \sim 0.8$ which are detected at both wavelengths (see Garn et al. 2009, for further details); converting this to a 1.4-GHz value using equation (4) of Garn & Alexander (2009), and assuming a radio spectral index of 0.8, we obtain a typical value of $q_{24} \equiv \log_{10}(S_{24}/S_{1.4}) = 0.8 \pm 0.4$ for star-forming galaxies at $z = 0.84$. We find that indeed most of the HiZELS radio emitters do cluster around $q_{24} \sim 0.7$, but four lie well away from this, with $q_{24} < 0.1$, and these are classified as ‘likely’ AGN.

3.5 Emission-line ratios

Spectroscopic data is available for 20 per cent of the COSMOS H α emitters from the z -COSMOS survey (Lilly et al. 2009), and Sobral et al. (2009a) used the [O II]3727/H β and [O III]5007/H β emission-line ratios to separate AGN from star-forming galaxies. 26 of the emitters had spectroscopy at sufficient SNR to carry out this comparison; of these sources, three (12 per cent) were classified by Sobral et al. (2009a) as likely AGN contaminants, and we retain that classification in this work. No spectroscopy is currently available for the UDS HiZELS sample, and as we do not have complete spectroscopy for the entire COSMOS sample, this value is a lower limit.

3.6 The AGN contamination rate at $z = 0.84$

Several of the H α emitters were classified as AGN under more than one criteria, and sources with two or more ‘possible’ classifications were considered to be ‘likely’ AGN candidates. In practice the distinction between ‘possible’ and ‘likely’ AGN candidates is only of interest in quantifying the uncertainty in the fraction of H α emitters which may be AGN; we do not use either of these types of source in later analysis. The total ‘possible’ and ‘likely’ AGN in each field were 20 and 22 (COSMOS) and 19 and 15 (UDS). We find a significantly different AGN fraction between the two fields (5 – 9 per cent in COSMOS, and 7 – 15 per cent in UDS). The principal cause of this discrepancy is the number of sources classified

as AGN through the IR colour-colour criteria; 10/464 (2.1 per cent) of COSMOS sources and 19/230 (8.3 per cent) of UDS sources fell within the Stern et al. (2005) region. We have placed more conservative errors on the UDS photometry as production of a band-merged catalogue is still ongoing – this leads to a higher fraction of UDS sources being ‘possible’ AGN than in COSMOS.

We visually inspected the SEDs of these sources in order to investigate this discrepancy – the majority showed a clear power-law AGN shape, and were also flagged as AGN under at least one other criteria, making it very likely that the classifications are correct. We believe that the bulk of the discrepancy between the two fields may be due to cosmic variance, although the slightly greater errors on the UDS photometry (which may incorrectly move a few sources into the AGN classification regions) may exaggerate this.

By combining the samples, we obtain an overall AGN contamination rate of between 5 and 11 per cent. The majority of sources classified as ‘possible’ AGN contaminants were best-fitted by an AGN template, but did not satisfy any of the specific colour requirements; for this reason, we believe that the true AGN contamination rate will be near to our quoted range. The variation in the number of sources detected by each technique suggests that (i) using a single criterion for starburst / AGN discrimination will underestimate the true AGN fraction, and (ii) a combination of colour-colour methods and full SED fitting should be used in order to maximise the success rate for AGN identification.

The technique of source stacking (used in Section 4) implicitly assumes that the sources being combined statistically are comparable to each other, but it is robust to the presence of a small number of outlier sources, such as AGN contaminants (see Garn & Alexander 2009, for further details). The results in the remainder of this work use only those sources that were not classified as either likely or possible AGN, but we have repeated all tests while retaining the possible AGN in our sample, and found no significant difference in any of the results. The H α and 24- μ m flux density of the AGN contaminants are very weakly correlated (see Section 4.1), and we believe that it is unlikely that any remaining AGN contaminants should have a significant effect on the results presented in this work.

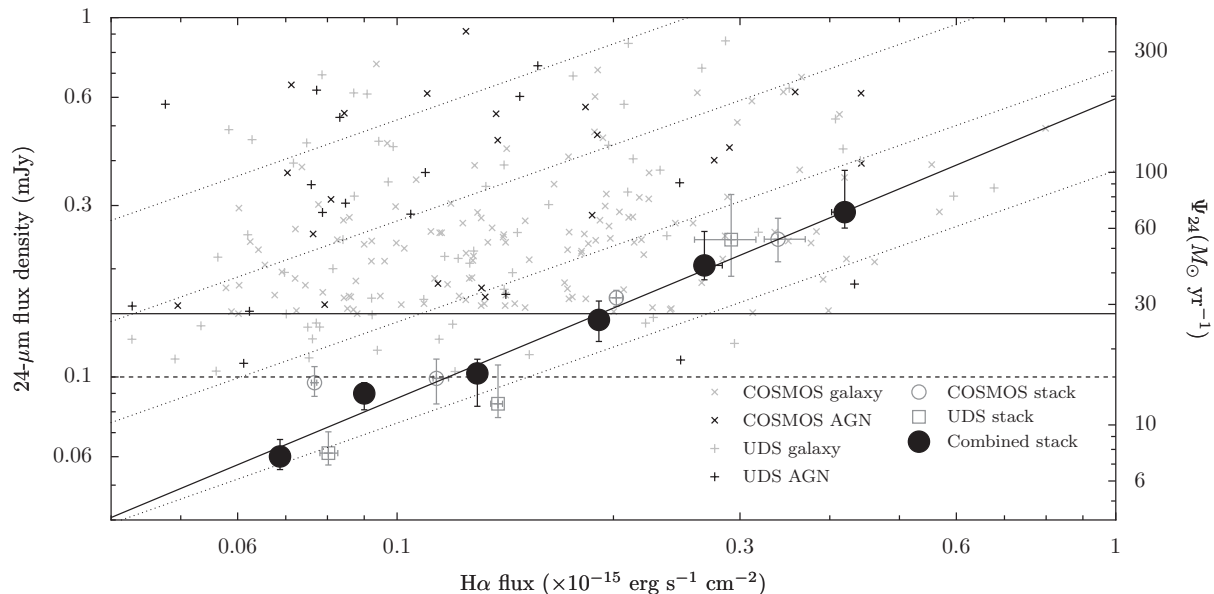


Figure 3. Variation in 24- μm flux density with $\text{H}\alpha$ flux, for the stacks of all $\text{H}\alpha$ emitters which were not flagged as AGN. The solid diagonal line represents the best-fitting relationship between 24- μm flux density and $\text{H}\alpha$ flux, with a power-law slope of 0.83. Individual $\text{H}\alpha$ emitters with 24- μm detections are indicated for comparison with the stacked data, separated by their AGN classification, and the COSMOS catalogue limit of 0.15 mJy ($\sim 7\sigma$) and UDS flux limit of 0.1 mJy are indicated by the horizontal solid and dashed lines respectively. Note that the filter profile correction, described in Section 4.1, has been applied to the stacked $\text{H}\alpha$ fluxes but not to the individual data points. The right-hand axis indicates the corresponding SFR for each 24- μm flux density, calculated using equation (2). The diagonal dotted lines represent the Kennicutt (1998) relationship between $\text{H}\alpha$ luminosity and SFR, modified by a factor of 0.66 in order to make the IMFs agree (see Section 4.2), and assuming an extinction of 1, 2, 3 and 4 mag (bottom to top).

4 ANALYSIS & RESULTS

4.1 Calculation of stacked 24- μm flux densities

It is necessary to know the locations of sources to within the size of a pixel (1.2 and 1.245 arcsec for the COSMOS and UDS 24- μm images respectively) in order to use source stacking. We have used source positions taken from the optical catalogues, which are expected to have an accuracy of about 0.2 arcsec (Capak et al. 2007; Furusawa et al. 2008), and we verified that there is no significant coordinate offset between the HiZELS data and their counterparts in the 24- μm images (median offsets in right ascension and declination of -0.04 ± 0.04 arcsec and 0.03 ± 0.04 arcsec for COSMOS sources, and -0.05 ± 0.08 arcsec and 0.30 ± 0.09 arcsec for UDS sources). The small positional offsets were not corrected for in later analysis.

The stacking technique used is very similar to that described in Garn & Alexander (2009), and further details and validation of the procedure can be found in that work. Sources were binned by their observed $\text{H}\alpha$ line flux, and a median $\text{H}\alpha$ flux calculated for each bin. A typical 24- μm flux density was then calculated for each set of binned data in two different ways:

(i) The 24- μm flux density of each $\text{H}\alpha$ emitter was measured within a circular aperture of 3 arcsec radius, centred on the source location. While individual flux density measurements are affected by the local 24- μm noise level, the statistical properties of the distribution give a robust estimate of the typical flux density for sources within the bin. The median was used as the statistical estimator, to avoid being biased by the combination of detected and undetected sources (see Garn & Alexander 2009, for further details), as for many stacks, the median flux density will come from individual detections at 24 μm (see Fig. 3).

(ii) A cut-out 24- μm image was created for each source in a bin, centred on the known HiZELS locations. From these cutouts, a stacked image was created, with each pixel calculated from the median of the values of the corresponding pixels of the cutout images. The flux density of the stacked image was then measured in the same way as for method (i). We experimented with the suggestion of Lonsdale et al. (2009) of placing images into a stack twice, once at 90° to the original orientation, in order to remove any systematic instrumental effects, but found that this made a negligible difference to the stacking results.

Measurements of the flux density obtained from random positions indicated the presence of a slightly negative background level in both images (approximately -0.01 MJy sr^{-1} , equating to a flux within a 3 arcsec radius of -8 μJy), which was subtracted from the flux density measurements to avoid biasing the stacking results.

The measured 24- μm flux density was multiplied by an aperture correction factor, obtained through comparison of the measured and catalogued flux densities of 24- μm sources within the COSMOS field, using a similar method to that in Garn & Alexander (2009). The calculated correction factor was 3.41 ± 0.12 , and should also be appropriate for UDS – the agreement between the stacked results from the two fields (see Fig. 3) implies that we are not introducing a systematic effect by using the COSMOS-derived aperture correction for the UDS stacking.

The narrow J -band filter used to identify $\text{H}\alpha$ emitters is not a perfect top-hat function, and this can have a measurable effect for sources with $\text{H}\alpha$ emission at wavelengths near the edge of the filter (as discussed in Sobral et al. 2009a). We calculate the statistical effect of this by simulating a distribution of 10^5 sources based upon the Sobral et al. (2009a) $\text{H}\alpha$ luminosity function. We spread them evenly in redshift over the range $z = 0.81 - 0.87$, and use the

actual filter profile to recover the luminosity distribution. Through comparison of the median input and median recovered luminosity, a statistical correction to the observed luminosity of each source was obtained – these corrections were applied to the $H\alpha$ data before stacking took place. The filter profile correction has a moderate effect on the faintest emitters (up to a ~ 20 per cent increase in luminosity), and little effect for the brightest emitters, as these can typically only be observed to be bright if they are not detected in low transmission regions of the filter. Nevertheless, all of the trends discussed in this work remain present if no correction is applied.

Error estimates for the $H\alpha$ fluxes and 24- μm stacked flux densities indicate the 68 percent confidence limits ($\pm 1\sigma$) obtained from the measured flux distribution (Gott et al. 2001). The flux densities obtained using both stacking methods were consistent to within 3 per cent, which we consider to be an additional uncertainty introduced through the stacking process, and add in quadrature to our error estimate. Throughout this work, all stacking results have been taken using method (i). The dominant errors on our stacked results come from the uncertainty in estimating stacked flux densities, due to the small number of galaxies in each bin (typically between ~ 20 and ~ 160).

4.2 Variation in 24- μm flux density or SFR with observed $H\alpha$ flux

Fig. 3 shows the stacked flux density measurements using the combined data from the COSMOS and UDS fields, with the results from each individual field also indicated for reference. While there is a strong correlation between the two stacked flux measurements, the relationship is significantly non-linear; the best-fitting power law has a slope of 0.83 ± 0.05 , and is indicated on Fig. 3. We have plotted individual $H\alpha$ emitters with 24- μm detections on Fig. 3, separated by their AGN classification, in order to investigate whether there is any strong dependence of 24- μm flux density on $H\alpha$ flux for the AGN sources with individual 24- μm detections – no such dependence is seen, with a Pearson product-moment correlation coefficient of $\rho = 0.29$, compared with $\rho = 0.55$ for the sources that are not classified as AGN.

Rieke et al. (2009) present a method for determining SFRs directly from *Spitzer* 24- μm flux density measurements. They assemble a series of template SEDs for galaxies with different luminosities, and create average SED templates which span the total IR luminosity range of $5 \times 10^9 - 10^{13} L_{\odot}$. From these bolometric luminosities, a SFR is calculated using a similar relationship to that in Kennicutt (1998). Each template is redshifted in steps of $\Delta z = 0.2$, and convolved with the MIPS 24- μm instrumental response function, in order to calculate the flux density which would be observed for the galaxy at a given redshift. The relationship between *observed* 24- μm flux density and SFR is parameterised at each discrete redshift, with the relationship at intermediate redshifts available through interpolation of the fit coefficients. The Rieke et al. (2009) parameterisation takes into account the variation in spectral shape (i.e. the K-correction) which is needed when converting from an observation-frame 24- μm flux density into a rest-frame 24- μm luminosity. Accurate knowledge of the K-correction is very important for 24- μm observations, which do not just probe the hot dust emission from the galaxy, but can also detect different polycyclic aromatic hydrocarbon features (PAH molecules; see e.g. Draine 2003) at varying redshifts.

At $z = 0.845$, the Rieke et al. (2009) relationship is

$$\log_{10} \left(\frac{\Psi_{24}}{M_{\odot} \text{ yr}^{-1}} \right) = 6.8795 + 1.4224 \times \log_{10} \left(\frac{S_{24}}{\text{Jy}} \right), \quad (2)$$

where S_{24} is the flux density measured within the 24- μm MIPS band, and we explicitly denote SFRs calculated from this band as Ψ_{24} . We have not included any systematic contribution to the errors from uncertainties in this conversion between flux density and SFR.

As with other methods of estimating SFR, there is an uncertainty due to the conversion between an observable parameter that comes principally from high-mass stars ($\gtrsim 5 M_{\odot}$, which carry out the majority of the dust heating), and a SFR which includes the rate of formation of much lower mass stars (down to $0.1 M_{\odot}$). The Initial Mass Function (IMF) used to convert between the two is typically assumed to be a single power-law slope of -1.35 from 0.1 to $100 M_{\odot}$ (Salpeter 1955), which can lead to an over-estimate of the number of low-mass stars which are forming. Rieke et al. (2009) use a modified IMF with a shallower slope at low mass (-0.3 from 0.08 to $0.5 M_{\odot}$ and -1.3 from 0.5 to $100 M_{\odot}$; Kroupa 2001) in order to calculate their SFR estimates, which results in a SFR that is a factor of 0.66 times the value which would be calculated from a Salpeter IMF containing the same mass of high-mass stars. This factor has already been applied to the Rieke et al. (2009) relationship in equation (2), and we adopt it throughout the remainder of this work where appropriate – in particular, to modify the Kennicutt (1998) SFR relationships, which were originally calculated using a Salpeter IMF. Error estimates on our results do not include any contribution from uncertainties in the IMF. However, all tracers of star formation that we consider in this work ($H\alpha$, UV, IR) are most sensitive to high-mass stars, and a change in assumed IMF at the low-mass end will make a very small difference to the overall conclusions, as it would alter the normalisation factors in the estimates of total SFR approximately equally at all wavelengths.

We indicate the SFRs that correspond to a given 24- μm flux density on Fig. 3, for reference. The diagonal lines indicate the Kennicutt (1998) relationship between $H\alpha$ flux and SFR, assuming different levels of extinction for all galaxies; as has been seen in previous works (e.g. Dopita et al. 2002), calculated extinction values vary significantly from galaxy to galaxy. The stacked data has a typical extinction of between 1 and 2 mag for all flux bins, and a visible increase for higher SFRs. Note that the individual galaxy detections are biased against low extinction (and therefore low 24- μm SFR) sources since only $H\alpha$ emitters with 24- μm counterparts are plotted – the stacked data has no such bias, as it uses both non-detections and sources individually detected at 24 μm .

4.3 Variation in $H\alpha$ extinction with observed $H\alpha$ luminosity

We can calculate the typical $H\alpha$ extinction for a bin of data, if we are willing to assume that 24- μm emission for an $H\alpha$ -selected sample is a reasonable SFR indicator, as was found by Rieke et al. (2009). We invert the Kennicutt (1998) relationship between SFR and $H\alpha$ luminosity (modified by a factor of 0.66 to make the IMFs consistent; see Section 4.2) to obtain a typical intrinsic $H\alpha$ luminosity, $L_{H\alpha, \text{int}}$, for each bin, i.e.

$$\left(\frac{L_{H\alpha, \text{int}}}{\text{erg s}^{-1}} \right) = 8.35 \times 10^{40} \left(\frac{\Psi_{24}}{M_{\odot} \text{ yr}^{-1}} \right). \quad (3)$$

As galaxies are all at a known redshift, these luminosities are converted to the observed line fluxes by assuming that a single value

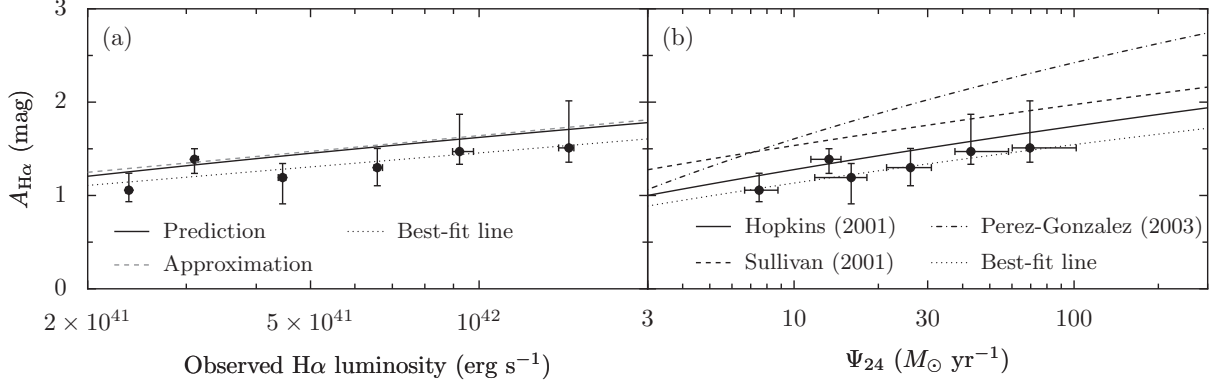


Figure 4. Variation in $H\alpha$ extinction for the $H\alpha$ emitters (black circles with error bars), after binning them by their observed $H\alpha$ flux. (a) Variation in extinction with observed $H\alpha$ luminosity (corrected for N II contamination but not for dust attenuation). The solid line shows the predicted relationship from equation (9), with the approximation from equation (10) shown by the dashed line. The best fit to the data, from equation (6), is indicated by the dotted line. (b) Variation in extinction with 24- μm SFR. The solid line shows the predicted relationship from equation (7), using the fit between the Balmer decrement and SFR from Hopkins et al. (2001), while the dashed and dash-dot lines are the equivalent relationships, using the fits from Sullivan et al. (2001) and Pérez-González et al. (2003) respectively – see Section 4.3 for further details. The best fit to the data, using the slope of equation (7) and $B = 5.8$, is shown by the dotted line. The hypothesis of a constant extinction for all $H\alpha$ luminosities or SFRs is excluded at the 3σ and 4σ level respectively.

of extinction $A_{H\alpha}$ can be applied to galaxies in each bin, i.e.

$$A_{H\alpha} = 2.5 \log_{10} \left(\frac{L_{H\alpha, \text{int}}}{4\pi d_L^2 S_{H\alpha}} \right), \quad (4)$$

where d_L is the luminosity-distance at $z = 0.845$. Combining these equations, we obtain

$$A_{H\alpha} = 2.5 \log_{10} \left[\left(\frac{8.35 \times 10^{40}}{4\pi d_L^2} \right) \left(\frac{\Psi_{24}/M_{\odot} \text{ yr}^{-1}}{S_{H\alpha}/\text{erg s}^{-1} \text{ cm}^{-2}} \right) \right]. \quad (5)$$

We calculate an extinction from each set of binned data using equation (5), and the results are shown on Fig. 4(a). There is an indication of an increase in $A_{H\alpha}$ with observed $H\alpha$ luminosity; the best fit to the data is

$$A_{H\alpha} = (-19.46 \pm 6.77) + (0.50 \pm 0.16) \log_{10} \left(\frac{L_{H\alpha, \text{obs}}}{\text{erg s}^{-1}} \right), \quad (6)$$

i.e. a 3σ detection of a variation in extinction with observed $H\alpha$ luminosity. However, if there is a dependence on luminosity (and by implication, on SFR activity) then relating extinction to observed $H\alpha$ luminosity may obscure some of the effects. In order to test this, we show the dependence of extinction on SFR in Fig. 4(b). The dependence of extinction on SFR is more prominent, with a best fit to the data of $A_{H\alpha} = (0.73 \pm 0.15) + (0.44 \pm 0.11) \log_{10}(\Psi_{24}/M_{\odot} \text{ yr}^{-1})$, i.e. a 4σ detection of SFR-dependent extinction.

Previous studies (e.g. Wang & Heckman 1996; Hopkins et al. 2001; Sullivan et al. 2001; Dopita et al. 2002; Berta et al. 2003; Pérez-González et al. 2003; Buat et al. 2005; Schmitt et al. 2006; Caputi et al. 2008) have found a correlation between extinction and either luminosity or SFR, with the implication being that more actively star-forming regions within a galaxy are also dustier. Hopkins et al. (2001) derived a SFR-dependent reddening relationship, based upon the observed Balmer decrement and far-IR luminosity of a sample of local star-forming galaxies (Wang & Heckman 1996). We repeat the derivation from Section 3 of Hopkins et al. (2001) in order to obtain a general expression for their relationship between SFR and extinction,

$$A_{H\alpha} = \frac{2.5k_{H\alpha}}{k_{H\beta} - k_{H\alpha}} \log_{10} \left[\frac{0.797 \log_{10}(\eta\Psi) + 3.83}{2.86} \right], \quad (7)$$

where k_{λ} is related to the $E(B - V)$ colour excess by $k_{\lambda} = A_{\lambda}/E(B - V)$, and $k_{H\alpha}$ and $k_{H\beta}$ are the values of k_{λ} at the wavelengths of $H\alpha$ and $H\beta$ radiation respectively. Ψ is the total SFR of a galaxy in $M_{\odot} \text{ yr}^{-1}$, and η is a conversion factor appropriate to the chosen IMF (1 for a Salpeter IMF, and 0.66 for the Kroupa IMF used in this work). The factor of η in equation (7) cancels an equivalent factor of $1/\eta$ during the calculation of Ψ from IR luminosity in Section 4.2, and is otherwise unimportant. The value of 2.86 represents the intrinsic $H\alpha/H\beta$ line flux ratio (appropriate for Case B recombination, a temperature of 10^4 K, and an electron density of 10^2 cm^{-3} ; Brocklehurst 1971), and the other numerical factors come from the least-squares fit performed by Hopkins et al. (2001) to the observed Balmer decrement and the logarithmic far-IR luminosity of local star-forming galaxies.

In order to test the form of the dust attenuation law, we assume that the numerical factors within the square brackets of equation (7) are fixed and correct, and fit our data for the numerical prefactor, $B \equiv 2.5k_{H\alpha}/(k_{H\beta} - k_{H\alpha})$, with errors coming from the typical uncertainty in $A_{H\alpha}$. We obtain $B = 5.8 \pm 1.0$, or alternately

$$\frac{k_{H\beta}}{k_{H\alpha}} = \left(1 + \frac{2.5}{B} \right) = 1.43 \pm 0.07. \quad (8)$$

This is consistent with the value obtained from the Calzetti et al. (2000) dust attenuation law, which predicts a value of $B = 6.54$, and gives $k_{H\beta}/k_{H\alpha} = 1.38$. We show this result on Fig. 4(b) to demonstrate the good agreement with our data. Values of B obtained from the individual fields are also consistent with this value (see Table 2).

Brinchmann et al. (2004) have tested the two assumptions that we have made in the derivation of equation (7), namely that the intrinsic $H\alpha/H\beta$ ratio is always equal to 2.86, and that the conversion between intrinsic $H\alpha$ luminosity and SFR that we use is appropriate for all galaxies. They conclude that while both assumptions are slightly flawed – the Case B ratio depends slightly upon temperature, while the most metal-rich galaxies produce a slightly lower $H\alpha$ luminosity for the same SFR – these variations are small and approximately cancel each other out; the combination of the two assumptions is therefore a fairly good approximation to make. Variations in the intrinsic Case B ratio for different temperatures (between a ratio of 2.72 and 3.03; Brocklehurst 1971) could only

affect our expected value of $B = 6.54$ by up to ± 0.16 , which is much smaller than the statistical errors in this study.

Sullivan et al. (2001) and Pérez-González et al. (2003) have also produced least-squares fits to the correlation between the Balmer decrement and $H\alpha$ -derived SFR from independent sets of galaxies, leading to slightly different numerical factors within the square brackets of equation (7). We show the equivalent versions of equation (7), calculated from these fits, on Fig. 4(b) for comparison with the Hopkins et al. (2001) result. As noted by Sullivan et al. (2001), the slope of their correlation is very similar to that of Hopkins et al. (2001), although the independent estimation of SFR from IR observations (carried out by Hopkins et al. 2001, and in this work), is preferable to using $H\alpha$ -derived values, providing that AGN contamination has been removed. We find that the slope of the Sullivan et al. (2001) relationship agrees with our data, but that the overall normalisation is too high. In contrast, the Pérez-González et al. (2003) correlation does not agree with our results; they indicate that if highly-obscured objects are removed from their sample, they find a correlation similar to that of Sullivan et al. (2001).

We note that Afonso et al. (2003) have found a significantly steeper relationship between SFR and $H\alpha$ extinction from a radio-selected sample than that obtained in this work or by Hopkins et al. (2001). However, while Hopkins et al. (2001) found a reasonable correlation between the Balmer decrement and IR luminosity of their sample, Afonso et al. (2003) did not find a good correlation between the Balmer decrement and radio-derived SFR of their sources, which may make their derived relationship less reliable.

Following Hopkins et al. (2001) we combine equations (3) and (7) to obtain a relationship between the extinction of a galaxy and its *observed* $H\alpha$ luminosity,

$$A_{H\alpha} = 12.8 \times 10^{A_{H\alpha}} - 2.5 \log_{10} \left[7.9 \times 10^{-42} \left(\frac{L_{H\alpha, \text{obs}}}{\text{erg s}^{-1}} \right) \right] - 12.0, \quad (9)$$

where the observed $H\alpha$ luminosity $L_{H\alpha, \text{obs}}$ is the value calculated from the observed $H\alpha$ line flux, after corrections for N II flux contamination, but before any dust attenuation correction has been applied to the data. Equation (9) cannot be solved analytically; however, over the luminosity range covered by sources in this study ($1.6 \times 10^{41} < L_{H\alpha, \text{obs}} < 4 \times 10^{42} \text{ erg s}^{-1}$), we can approximate it by the linear fit

$$A_{H\alpha} = -21.963 + 0.562 \log_{10} \left(\frac{L_{H\alpha, \text{obs}}}{\text{erg s}^{-1}} \right). \quad (10)$$

This is consistent with our fit to the data from equation (6), as shown on Fig. 4(a), and is within 5 per cent of the numerical solution over the observed luminosity range tested in this work. The approximate and numerical solutions are consistent to within 10 per cent over the luminosity range of $10^{41} - 10^{44} \text{ erg s}^{-1}$.

4.4 Dependence of $H\alpha$ extinction on galaxy properties

We have shown that equation (7) is appropriate for our full sample of $H\alpha$ emitters, and accurately describes the variation in dust extinction for sources with different SFRs. In order to test whether there is any variation in dust attenuation between different types of galaxies, we split the sample into subsets based upon other properties of the galaxies. We stack each subset into different $H\alpha$ flux bins in order to remove the dependence of extinction on SFR, as the mean SFR of different galaxy types can vary strongly. We then repeat the analysis of Section 4.3 in order to verify that equation (7)

Table 2. The calculated values of normalisation B and error σ_B for equation (7), broken down by the source selection criteria. The number of galaxies that satisfied a particular selection criteria, N , is listed for reference – if N was not large enough for meaningful statistics, no normalisation is given.

Sample	N	B	σ_B
All $H\alpha$ emitters	618	5.8	1.0
COSMOS	422	6.2	0.8
UDS	196	4.9	1.5
COSMOS:			
disk / spiral morphology	347	6.9	0.7
irregular morphology	57	6.3	2.4
early-type morphology	12	-	-
disk / spiral, disk-dominated	117	6.5	1.1
disk / spiral, intermediate	155	7.3	0.7
disk / spiral, bulge-dominated	21	-	-
merging	92	6.0	1.9
not merging	291	6.9	0.7
low-density	207	6.8	0.8
high-density	207	6.3	0.9
$9.5 < \log_{10}(\text{stellar mass}/M_{\odot}) < 9.8$	67	1.6	1.6
$9.8 < \log_{10}(\text{stellar mass}/M_{\odot}) < 10.1$	141	4.6	0.9
$10.1 < \log_{10}(\text{stellar mass}/M_{\odot}) < 10.4$	180	6.6	0.6
$10.4 < \log_{10}(\text{stellar mass}/M_{\odot}) < 10.7$	135	7.8	0.7
$10.7 < \log_{10}(\text{stellar mass}/M_{\odot}) < 11.0$	57	6.8	2.7
Predicted value from Calzetti et al. (2000)		6.54	

accurately describes the variations in the data, and to calculate a value of B for the subset. A summary of the relationships derived for all subsets of galaxies can be found in Table 2.

4.4.1 Morphological type

A large *Hubble Space Telescope* survey of the full 1.8 deg^2 COSMOS field has been completed (Scoville et al. 2007b), producing images with ~ 0.1 arcsec resolution. Morphological classifications have been performed on ~ 40 per cent of the field (Scarлата et al. 2007), and the majority of the $H\alpha$ emitters have been assigned a source type (disk/spiral, irregular, early-type) by Sobral et al. (2009a), based upon this morphological classification, visual inspection, and colours taken from the Subaru optical data. There are too few early-type galaxies in the sample for a meaningful comparison, but the disk/spiral and irregular galaxies are shown in Fig. 5(a).

Scarлата et al. (2007) have further classified the galaxies with a disk/spiral morphological type by their bulge-to-disk ratio. The number of bulge-dominated galaxies is too small for a meaningful comparison, but no significant difference is seen between the intermediate and disk-dominated galaxies in Fig. 5(b).

4.4.2 Merger activity

Sobral et al. (2009a) have visually inspected the galaxies and classified them according to whether they are undergoing mergers (93 galaxies), or definitely not merging (292 galaxies). The remaining galaxies were potential mergers; we have not included these in the analysis as it is unclear which class they should belong to. The merging galaxies and non-merging galaxies are shown on Fig. 5(c).

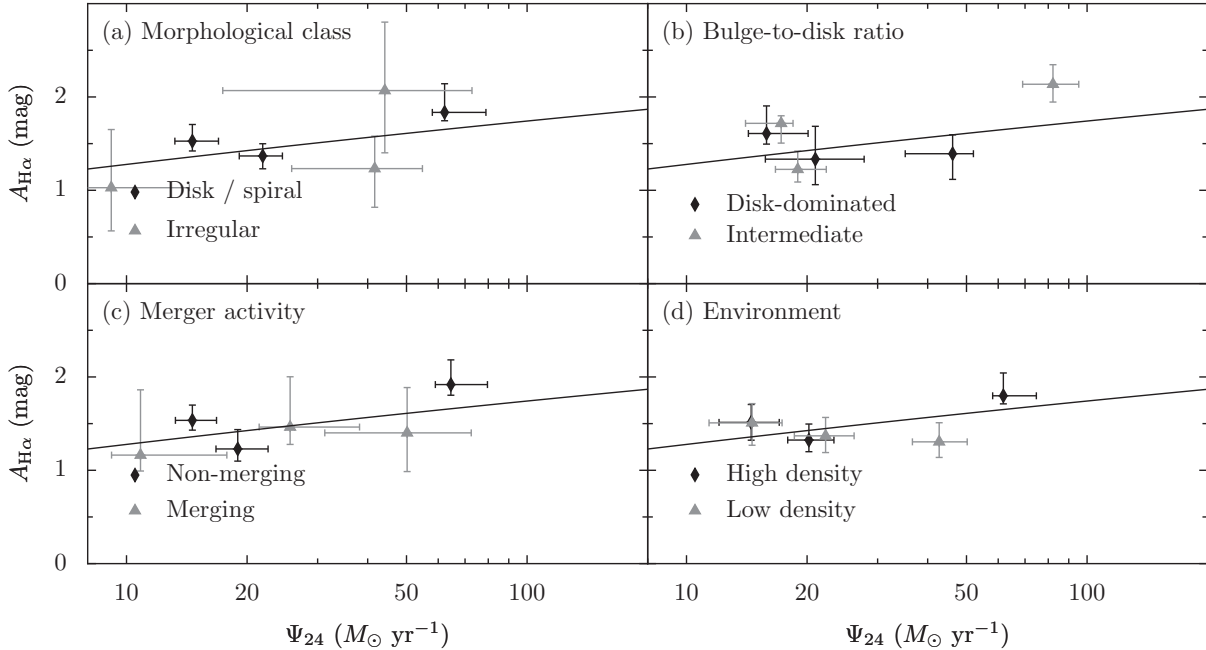


Figure 5. The relationship between $H\alpha$ extinction and SFR, for various subsets of the COSMOS data – the meaning of each classification can be found in Section 4.4. The diagonal lines show the predicted relationship between $A_{H\alpha}$ and SFR from equation (7) using $B = 6.54$, and are not fitted to the data. Values of B obtained through fitting equation (7) can be found in Table 2, along with errors for each fit.

4.4.3 Environment

The angular distances to all nearby sources at comparable redshift have been calculated for each $H\alpha$ emitter, and converted into a linear distance to the 10th-nearest neighbour, r_{10} (D. Sobral et al., in preparation). From these distances, a local projected surface density can be calculated using $\Sigma = 10/\pi r_{10}^2$. We split the sample in half according to the local density; as shown in Fig. 5(d), no significant difference is seen between the two subsets.

4.4.4 Stellar mass

Stellar mass estimates are available for all COSMOS and UDS sources (Mobasher et al. 2007, M. Cirasuolo et al., in preparation). We split our sample in half by stellar mass, as shown in Fig. 6(a). Two results are apparent from this plot – bins with lower stellar mass also have a lower median SFR, and the lowest stellar mass bin appears to have a decreased normalisation compared with the higher mass bin.

Previous studies have shown that the stellar mass and SFR of a galaxy are correlated (e.g. Brinchmann et al. 2004), and the first of our results is consistent with these studies. In order to investigate the second result further, we divide our sample into five stellar mass bins (and three $H\alpha$ flux bins), calculate normalisations for each sub-sample, and use equation (7) to predict the extinction that would be obtained for a galaxy of this stellar mass, and a SFR of $10 M_{\odot} \text{ yr}^{-1}$. These extinctions are shown in Fig. 6(b). We find that galaxies with stellar mass above $\sim 10^{10.2} M_{\odot}$ have an approximately constant extinction / SFR relationship (i.e. for a given SFR, the predicted extinction would be the same), but that below this stellar mass, the typical extinction for a galaxy with given SFR decreases significantly. This may be a result of incompleteness in our sample, based upon the stellar mass distribution of our $H\alpha$ emitters (which we find to peak at $\sim 10^{10.2} M_{\odot}$). We do

however note that Brinchmann et al. (2004) have detected a dependence of $H\alpha$ extinction on stellar mass for galaxies within SDSS, which they attribute to a correlation between mass and metallicity for star-forming galaxies. Their results do not take into account the dependence of extinction on SFR which we have confirmed in this work, and so may simply be a consequence of a correlation between SFR and stellar mass for star-forming galaxies. We defer further investigation of this relationship to a separate work (Garn et al. in preparation).

4.4.5 Summary

With the exception of the potential stellar mass dependence, we find no statistically significant difference between the normalisations of the relationship between extinction and SFR for any of these subsets of galaxies, as shown in Table 2 and Fig. 5. This may simply be a consequence of the limited number of galaxies available – after splitting the COSMOS galaxies into two or three classifications, and a further three $H\alpha$ flux bins, there are only typically a few tens of galaxies contained within each bin, and any difference would have to be very large in order to be detectable. Note that plots of extinction against observed luminosity (not shown) also indicate that there is no significant difference between the various subsets, but we have chosen to illustrate this fact by relating the extinction to 24- μm -estimated SFR rather than to observed $H\alpha$ luminosity, so that a direct comparison to the results of Hopkins et al. (2001) can be made.

We conclude that within the uncertainties quoted in Table 2, the relationship between extinction and SFR that was presented in equation (7) is appropriate for use in galaxies with a wide range of morphologies and properties.

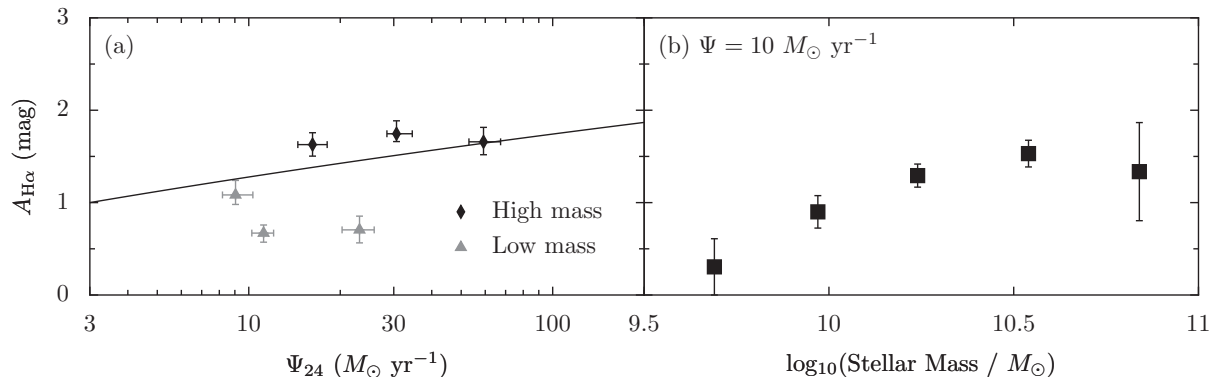


Figure 6. The relationship between H α extinction and SFR for data binned by stellar mass. (a) Data separated into two stellar mass bins. (b) The extinction that would be predicted for a galaxy of a given stellar mass, and a SFR of $\Psi = 10 M_{\odot} \text{ yr}^{-1}$, with the data separated into five mass bins.

Table 3. The rest-frame wavelength, zero-point correction and median galactic extinction for each of the three bands used to calculate the UV extinction, along with the calculated conversion factor γ between nebular and stellar reddening for each band from equation (13), using the stacked data (Fig. 7), and from individual sources (Fig. 8).

	u^*	B_J	g^+
Rest-frame λ (\AA)	2058.5	2417.2	2590.6
Zero-point correction	-0.084	0.189	-0.090
Galactic extinction	-0.086	-0.074	-0.069
γ (stacked data)	0.50 ± 0.07	0.50 ± 0.07	0.48 ± 0.07
γ (individual sources)	0.49 ± 0.14	0.49 ± 0.14	0.47 ± 0.14

4.5 UV dust extinction

The UV luminosity of a galaxy is also produced directly from young, high-mass stars, and will be attenuated by interstellar dust. We estimate the dust extinction in the rest-frame UV, A_{UV} , in a similar manner to Section 4.3. As before, we assume that Ψ_{24} is a good proxy for the true total SFR, and use an IMF-modified version of the Kennicutt (1998) calibration to calculate a typical UV luminosity, L_{ν} , for each bin, through

$$\left(\frac{L_{\nu}}{\text{W Hz}^{-1}} \right) = 4.71 \times 10^{20} \left(\frac{\Psi_{24}}{M_{\odot} \text{ yr}^{-1}} \right). \quad (11)$$

A_{UV} is then estimated through comparison of L_{ν} and an observed flux density, S_{ν} , using

$$A_{\text{UV}} = 2.5 \log_{10} \left[\frac{L_{\nu}(1+z)}{4\pi d_L^2 S_{\nu}} \right], \quad (12)$$

where the $1+z$ factor accounts for bandwidth stretching.

We have three photometric bands that trace far-UV flux density (u^* , B_J and g^+), with the rest-frame wavelengths that they probe listed in Table 3. We only consider COSMOS galaxies in this section, as there are currently no accurate photometric corrections available for the UDS data. We applied the photometric zero-point corrections that are recommended by Capak et al. (2007) to the photometry of each source, along with individual corrections for galactic extinction (with the median correction factors listed in Table 3). An appropriate aperture correction (which applies to each band; see Capak et al. 2007) was taken from the PSF-matched catalogue for each source, with a median correction of -0.275 mag.

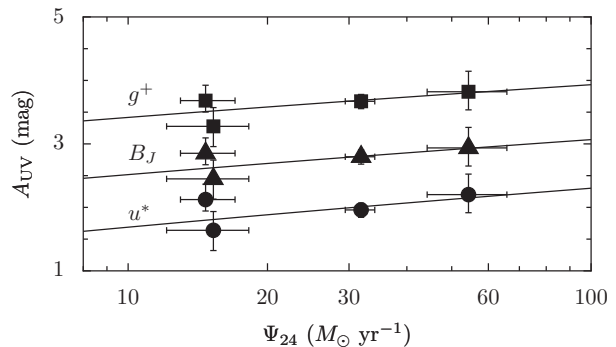


Figure 7. Variation in the median UV extinction with 24- μm SFR, for the HiZELS COSMOS emitters after selection by their H α flux. The UV extinction has been calculated from photometry in the u^* band, B_J band (offset by +1 mag) and g^+ band (offset by +2 mag). The solid lines are fits to equation (13), using the Calzetti et al. (2000) dust attenuation law to calculate k_{UV} , and with values of γ as listed in Table 3.

Fig. 7 shows the measured dependence of UV extinction on SFR for the three bands – as before, there is a correlation between the SFR and UV extinction.

Calzetti (1997) found that the dust obscuration of stellar continuum emission between the wavelengths of the H α and H β lines is less than would be expected from an extrapolation of the obscuration of the line emission. They found that the optical depth of the dust that was obscuring the continuum was about 60 per cent of the depth of the dust that obscures the line emission. The inference drawn from this was that massive stars (producing the H α /H β emission) form in dusty environments, while the bulk of the red stellar continuum was a result of much less dust-obscured stars (presumably older, and lower mass), at a different location in the galaxy. They suggest using $E(B-V)_{\text{star}} = (0.44 \pm 0.03) \times E(B-V)_{\text{gas}}$ to calculate the reddening of the continuum emission.

The difference of environment should not be true for H α and UV continuum radiation, which are both predominantly produced by the same population of young stars; it might therefore be expected that the correction factor (which we denote as γ) should converge to 1 for shorter wavelength continuum radiation, where the obscuring dust will become more like the dust that obscures the H α emission. Note, however, that the value of γ is closely linked to the shape of the Calzetti et al. (2000) dust law, which has been calculated through comparisons of the SEDs of attenuated galaxies

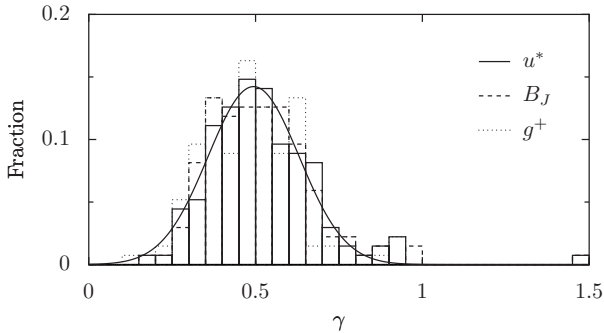


Figure 8. The distribution of γ for COSMOS H α emitters with individual detections at 24- μ m, calculated from the u^* , B_J and g^+ bands. The Gaussian is a fit to the u -band data, with $\bar{\gamma} = 0.50$ and $\sigma = 0.14$.

and their unattenuated counterparts – different wavelength regions of the dust attenuation law relate to different regions of a galaxy (i.e. the UV end is physically related to the dusty star-forming regions, while the long wavelength end will be weighted towards the old stellar population residing in less dusty regions). As such, there is a degeneracy between the wavelength dependence of γ and k_λ that does not relate to physical properties of dust within galaxies. We therefore believe that while the value of γ is useful in calculating UV attenuation from the Balmer decrement and vice versa, it does not have a direct physical relevance, as it is closely linked with the assumed form of the dust law. If UV extinction at $z = 0.84$ is the same as that seen locally, and described by the Calzetti et al. (2000) dust law, we would expect to find $\gamma \approx 0.44$ for UV emission as well as for longer wavelength continuum emission.

We allow the conversion between nebular and stellar reddening, γ , to be a free parameter, and adjust equation (7) by this factor to obtain

$$A_{UV} = \frac{2.5\gamma k_{UV}}{k_{H\beta} - k_{H\alpha}} \log_{10} \left[\frac{0.797 \log_{10}(\eta\Psi) + 3.83}{2.86} \right], \quad (13)$$

where k_{UV} is the dust attenuation at the rest-frame wavelength of interest. We fit for γ by assuming that the Calzetti et al. (2000) dust attenuation law accurately estimates k_{UV} (which we verify through a comparison of the results from different bands), and show these fits on Fig. 7. The values of γ are given in Table 3 – all are larger than 0.44, but are within $\sim 1\sigma$ of the Calzetti (1997) result.

We calculate the H α and UV extinction for each of the 134 COSMOS H α emitters with a 24- μ m counterpart in the MIPS catalogue, that were not flagged as AGN. A strong correlation is seen between $A_{H\alpha}$ and each of the A_{UV} measurements (with $\rho = 0.70$), and from these extinctions we calculate γ on a source-by-source basis. The distribution of γ is shown in Fig. 8, and the results given in Table 3 – in each case the data is consistent with a Gaussian centred on 0.5, with $\sigma = 0.14$. A two-sample Kolmogorov-Smirnov test confirms that no significant difference is seen between the distributions of γ in the three bands. We therefore conclude that $\gamma = 0.50 \pm 0.14$, i.e. the dust attenuation of UV emission is approximately half of that which would be predicted from a simple extrapolation of nebular reddening using the Calzetti et al. (2000) dust attenuation law. This is in agreement with the low-redshift result, and implies that the Calzetti et al. (2000) law is broadly applicable to our galaxies.

The principal qualitative difference between the Calzetti et al. (2000) dust attenuation law, derived from local starburst galaxies, and the individual extinction laws measured from observations of

stars within the Milky Way or the Large Magellanic Cloud is the absence of a ‘bump’ at around 2175 Å in the rest-frame UV. There is a conceptual difference between dust ‘extinction’ by an intervening dust cloud, and dust ‘attenuation’ from an extended source by a distribution of dust that is mixed with the stars (see Calzetti 1997, for more details). However, Gordon, Calzetti & Witt (1997) have shown that it is not possible to explain the absence of a 2175 Å dust feature purely through geometrical effects, implying that the lack of this feature is intrinsic to the properties of dust grains within local starburst galaxies.

There are indications that a few high-redshift sources may contain this dust feature (e.g. Solórzano-Iñarrea et al. 2004; Srianand et al. 2008; Elíasdóttir et al. 2009; Noterdaeme et al. 2009). A 2175 Å bump would show up prominently in our data, via a greater extinction in the u^* -band data than in the B_J and g^+ bands. As no such difference has been found, we conclude that the dust attenuation law of high-redshift star-forming galaxies does not require the addition of a UV bump.

5 DISCUSSION

5.1 Variation in H α dust extinction with SFR

H α emission is an excellent tracer to use for cosmic SFR studies as it is sensitive, can be easily studied over large volumes, and has a clean selection function. However, it is necessary to correct the observed H α luminosity for the effects of dust extinction before the true SFR can be obtained.

We have shown in Section 4 that the empirical relationship between the SFR of local galaxies and their H α extinction is also appropriate for galaxies at $z = 0.84$. We have further split our sample of galaxies by their morphological type, bulge-to-disk ratio, merger activity and the local density of their environments. No statistically significant difference was seen in the normalisations of the SFR / H α extinction relationship, implying that this is a general property of galaxies which applies at least over the range $0 < z < 0.84$, to spiral and irregular galaxies, disk-dominated galaxies and galaxies with a moderate bulge component, to galaxies that are and are not undergoing merger activity, and galaxies in high and low density environments.

The increase in extinction with higher SFR can be explained through the fact that star formation takes place within dusty molecular clouds, and the SFR is related to the gas surface density (the Schmidt-Kennicutt law; Schmidt 1959; Kennicutt 1989) – more actively star-forming regions are likely to have dustier environments, where the H α luminosity produced by young stars will suffer a greater amount of attenuation.

Equation (7) allows us to estimate the typical extinction that is appropriate for galaxies with different SFRs; the value of $A_{H\alpha} = 1$ mag – commonly taken to be the amount of dust extinction to correct for – is appropriate for galaxies with a SFR of $\sim 3 M_\odot \text{ yr}^{-1}$, comparable to the typical rates of star formation in the local Universe. The typical extinction that is appropriate for galaxies with a SFR of 10 and $100 M_\odot \text{ yr}^{-1}$ is ~ 1.3 and ~ 1.7 mag, although extinctions calculated for individual galaxies may vary considerably from these values. Dopita et al. (2002) find a range of H α extinctions between ~ 1 and 3 for galaxies with SFR of $\sim 100 M_\odot \text{ yr}^{-1}$, and Fig. 3 shows a similar spread of IR-derived H α extinctions for individual sources.

5.2 Variation in H α dust extinction between $0 < z < 0.84$

Several works (e.g. Tresse et al. 2007; Villar et al. 2008) find that the amount of dust extinction is greater at high redshift than in the local Universe, with Villar et al. (2008) obtaining a mean extinction of $A_{\text{H}\alpha} = 1.48$ mag from a sample of H α emitters at $z = 0.84$. We also find this increase, with a typical extinction value within 1σ of 1.5 mag; however, our results from this section and Section 4.3 demonstrate that this merely reflects the greater number of high-SFR sources at higher redshift, rather than an intrinsic increase in extinction for similar galaxies at the two redshifts. We have excluded the possibility of there being no dependence of H α extinction on SFR at the 4σ level, a conclusion that is in agreement with the results of Choi et al. (2006) and Caputi et al. (2008), who find that variations in V-band extinction for different galaxies are correlated with luminosity, rather than with redshift.

The typical extinction that is measured from a survey that detects H α emitters at a specific redshift will be dependent on the detection threshold – counter-intuitively, a deeper survey will lead to a lower measurement of the average extinction, since from Fig. 4, a lower luminosity threshold also implies a lower extinction threshold. We use this result to caution against drawing conclusions about the typical dust extinction of galaxies at a given redshift, without taking into account any SFR dependency.

5.3 The effect of variable extinction on the H α luminosity function and star formation rate density at $z = 0.84$

Sobral et al. (2009a) presented an extinction-corrected H α luminosity function at $z = 0.84$ from the HiZELS data used in this work. A single extinction of $A_{\text{H}\alpha} = 1$ mag was used to correct all sources, and a Schechter function was fitted to the data, yielding values of L^* , ϕ^* and α which are presented in column 1 of Table 4.

We recalculate the H α luminosity function at $z = 0.84$ from all H α emitters, applying the extinction correction from equation (10), and obtain new values of L^* , ϕ^* and α , listed in column 2 of Table 4. These results remain consistent with strong evolution in L^* and ϕ^* over the range $0 < z < 1$, as found in Sobral et al. (2009a). The most significant change is an increase in the characteristic turnover luminosity, L^* ; the increase in the typical H α extinction leads to a greater number density of bright emitters, compared with taking $A_{\text{H}\alpha} = 1$ mag for all sources.

Sobral et al. (2009a) calculated the average star formation rate density (SFRD) at $z = 0.84$, by integrating the luminosity function and applying an average 15 per cent correction for AGN contamination. If we use a variable H α extinction correction, and simply apply a 15 per cent AGN contamination correction, we obtain a significantly larger value for the SFRD than that found from using 1 mag of extinction (column 2 of Table 4). However, we can improve upon this estimate by recalculating the H α luminosity function, excluding those sources which were classified as potential AGN (column 3 of Table 4). There is a flattening seen towards the faint end of the luminosity function, with α consistent with a value of -1.4 . We integrate this luminosity function down to the limit of the HiZELS survey, $L_{\text{H}\alpha} = 10^{41.5}$ erg s $^{-1}$, and obtain a SFRD of $0.15 \pm 0.01 M_{\odot} \text{ yr}^{-1} \text{ Mpc}^{-3}$, essentially identical to the value obtained by Sobral et al. (2009a) of $0.15 \pm 0.02 M_{\odot} \text{ yr}^{-1} \text{ Mpc}^{-3}$. By integrating the entire luminosity function, we obtain a SFRD of $0.32 \pm 0.12 M_{\odot} \text{ yr}^{-1} \text{ Mpc}^{-3}$, compared with the value from Sobral et al. (2009a) of $0.37 \pm 0.18 M_{\odot} \text{ yr}^{-1} \text{ Mpc}^{-3}$. The combination of an improved AGN identification method and variable

Table 4. Schechter function parameters L^* , ϕ^* and α for the $z = 0.84$ H α luminosity function, along with the average SFRD (in $M_{\odot} \text{ yr}^{-1} \text{ Mpc}^{-3}$) obtained by integrating the luminosity function down to the HiZELS survey limit of $L_{\text{H}\alpha} = 10^{41.5}$ erg s $^{-1}$, or across the total luminosity range. The H α extinction assumed when calculating the luminosity function is either ‘1 mag’ (Sobral et al. 2009a) or ‘Variable’ (the results from this work), and the AGN correction applied when calculating the SFRD either uses all H α emitters to calculate the luminosity function and then assumes a 15 per cent contamination fraction, or only uses those emitters which were not identified as AGN.

Corrections:			
Extinction	1 mag	Variable	Variable
AGN	15 per cent	15 per cent	AGN excluded
Parameter:			
$\log_{10}(L^*/\text{erg s}^{-1})$	42.26 ± 0.05	42.50 ± 0.04	42.44 ± 0.05
$\log_{10}(\phi^*/\text{Mpc}^{-3})$	-1.92 ± 0.10	-2.05 ± 0.09	-1.99 ± 0.10
α	-1.65 ± 0.15	-1.60 ± 0.10	-1.40 ± 0.20
SFR density:			
$> 10^{41.5}$ erg s $^{-1}$	0.15 ± 0.02	0.24 ± 0.05	0.15 ± 0.01
Total	0.37 ± 0.18	0.41 ± 0.16	0.32 ± 0.12

dust attenuation only has a moderate effect on the calculated SFRD at $z = 0.84$, although may be more important at higher redshift.

6 CONCLUSIONS

We have used a well-defined sample of H α -emitting galaxies at $z = 0.84$ to study the link between star formation and dust extinction. The HiZELS sample consisted of 694 H α -emitting galaxies within the redshift range $z = 0.845 \pm 0.021$ in the well-studied COSMOS and UDS fields, with additional information available in multiple UV, optical and IR bands, along with ancillary radio and X-ray data.

In order to focus on star-forming galaxies, it was necessary to remove AGN contaminants from our sample. We performed this removal through a number of multi-wavelength classification methods; emission-line diagnostics, deviations away from the IR / radio correlation, X-ray counterparts, mid-IR and mid- to far-IR shapes and full template fitting were all used to identify potential AGN. We estimate an AGN contamination rate of between 5 and 11 per cent for H α -selected emission-line sources at $z = 0.84$. No single diagnostic identified more than half of the AGN contaminants, with SED template fitting being the most successful; we suggest that using a combination of template-fitting and colour-colour diagnostics will maximise the success rate of AGN identification in H α surveys.

In order to constrain the average IR luminosity of H α emitters at $z = 0.84$, we have binned our sample by observed H α flux, and used the technique of source stacking to calculate typical 24- μm flux densities for the H α emitters. Several previous studies have found that dust extinction correlates with either luminosity or SFR, and we looked for a relationship between the SFR of a galaxy and its dust attenuation. We found that individual extinctions vary significantly between galaxies, but confirm that this correlation holds for the average properties of our sample; galaxies with higher SFR also undergo a greater amount of extinction.

We have presented an approximate method of calculating the typical H α extinction of a galaxy, based solely upon the observed H α luminosity; $A_{\text{H}\alpha} = -21.963 + 0.562 \log_{10}(L_{\text{H}\alpha,\text{obs}}/\text{erg s}^{-1})$,

which is within 10 per cent of the full numerical solution over the luminosity range $10^{41} - 10^{44}$ erg s^{-1} . This is found to describe the properties of galaxies with disk, spiral and irregular morphologies, a range of bulge-to-disk ratios, galaxies in high- and low-density environments, and both merging and non-merging galaxies, although a potential deviation in this relationship may be seen for galaxies with low stellar masses. We emphasize that this is only an average relationship, and that the extinction measured within individual galaxies can vary away from this relationship by up to ~ 2 mag.

We have calculated the far-UV extinction of galaxies in a similar manner to the $H\alpha$ extinction, and found a qualitatively similar correlation between this extinction and the SFR. We find that the UV dust obscuration is about half of that expected from an extrapolation of the Calzetti et al. (2000) dust attenuation law. By calculating UV extinctions from flux densities measured in three different bands, we show that, similar to the local Universe, there is no evidence for a 2175 Å UV bump in the dust attenuation of high-redshift star-forming galaxies.

The relationship between dust extinction and SFR at $z = 0.84$ is the same as is seen at $z \sim 0$; we conclude that there is no evidence for a change in the dust properties of galaxies over this redshift range, and that any average increase in the extinction of galaxies at higher redshift is due to the overall increase in star formation activity out to $z \sim 2$. Using our relationship between observed $H\alpha$ luminosity and extinction, we recalculate the $H\alpha$ luminosity function for galaxies at $z = 0.84$. We find an increase in the characteristic luminosity compared with the value obtained by assuming a single value of extinction is applicable to all sources, implying a greater number density of bright $H\alpha$ emitters than previous estimates at $z = 0.84$.

ACKNOWLEDGEMENTS

TSG and PNB are grateful for support from the Leverhulme Trust. DS would like to thank the Fundação para a Ciência e Tecnologia (FCT) for the doctoral fellowship SFRH/BD/36628/2007. JEG and IRS acknowledge support from STFC. RJM and JSD acknowledge the support of the Royal Society through a University Research Fellowship and a Wolfson Research Merit award respectively. DF thanks STFC for support via an Advanced Fellowship.

REFERENCES

- Abazajian K. N., et al., 2004, *AJ*, 128, 502
 Afonso J., Hopkins A., Mobasher B., Almeida C., 2003, *ApJ*, 597, 269
 Appleton P. N., et al., 2004, *ApJS*, 154, 147
 Bauer F. E., Alexander D. M., Brandt W. N., Schneider D. P., Treister E., Hornschemeier A. E., Garmire G. P., 2004, *AJ*, 128, 2048
 Bell E. F., Kennicutt R. C., 2001, *ApJ*, 548, 681
 Berta S., Fritz J., Franceschini A., Bressan A., Pernechele C., 2003, *A&A*, 403, 119
 Bondi M., Ciliegi P., Schinnerer E., Smolčić V., Jahnke K., Carilli C., Zamorani G., 2008, *ApJ*, 681, 1129
 Brinchmann J., Charlot S., White S. D. M., Tremonti C., Kauffmann G., Heckman T., Brinkmann J., 2004, *MNRAS*, 351, 1151
 Brocklehurst M., 1971, *MNRAS*, 153, 471
 Buat V., et al., 2005, *ApJ*, 619, L51
 Calzetti D., 1997, *AJ*, 113, 162
 Calzetti D., Armus L., Bohlin R. C., Kinney A. L., Koornneef J., Storchi-Bergmann T., 2000, *ApJ*, 533, 682
 Capak P., et al., 2007, *ApJS*, 172, 99
 Cappelluti N., et al., 2009, *A&A*, 497, 635
 Caputi K. I., et al., 2008, *ApJ*, 680, 939
 Chapman S. C., Blain A. W., Smail I., Ivison R. J., 2005, *ApJ*, 622, 772
 Charlot S., Kauffmann G., Longhetti M., Tresse L., White S. D. M., Maddox S. J., Fall S. M., 2002, *MNRAS*, 330, 876
 Choi P. I., et al., 2006, *ApJ*, 637, 227
 Condon J. J., 1992, *ARA&A*, 30, 575
 Condon J. J., Yin Q. F., 1990, *ApJ*, 357, 97
 Dale D. A., Helou G., Contursi A., Silbermann N. A., Kolhatkar S., 2001, *ApJ*, 549, 215
 Dopita M. A., Pereira M., Kewley L. J., Capaccioli M., 2002, *ApJS*, 143, 47
 Draine B. T., 2003, *ARA&A*, 41, 241
 Elíasdóttir Á., et al., 2009, *ApJ*, 697, 1725
 Elvis M., et al., 2009, *ApJS*, 184, 158
 Fujita S. S., et al., 2003, *ApJ*, 586, L115
 Furusawa H., et al., 2008, *ApJS*, 176, 1
 Garn T., Alexander P., 2009, *MNRAS*, 394, 105
 Garn T., Green D. A., Riley J. M., Alexander P., 2009, *MNRAS*, 397, 1101
 Geach J. E., Smail I., Best P. N., Kurk J., Casali M., Ivison R. J., Coppin K., 2008, *MNRAS*, 388, 1473
 Gordon K. D., Calzetti D., Witt A. N., 1997, *ApJ*, 487, 625
 Gott R. J., Vogeley M. S., Podariu S., Bharat R., 2001, *ApJ*, 549, 1
 Hopkins A. M., Beacom J. F., 2006, *ApJ*, 651, 142
 Hopkins A. M., Connolly A. J., Haarsma D. B., Cram L. E., 2001, *AJ*, 122, 288
 Kennicutt R. C., 1983, *ApJ*, 272, 54
 Kennicutt R. C., 1989, *ApJ*, 344, 685
 Kennicutt R. C., 1998, *ARA&A*, 36, 189
 Kroupa P., 2001, *MNRAS*, 322, 231
 Lawrence A., et al., 2007, *MNRAS*, 379, 1599
 Le Floch E., et al., 2009, *ApJ*, 703, 222
 Lilly S. J., et al., 2009, *ApJS*, 184, 218
 Lonsdale C. J., et al., 2009, *ApJ*, 692, 422
 Ly C., et al., 2007, *ApJ*, 657, 738
 Mobasher B., et al., 2007, *ApJS*, 172, 117
 Moustakas J., Kennicutt R. C., Tremonti C. A., 2006, *ApJ*, 642, 775
 Noterdaeme P., Ledoux C., Srianand R., Petitjean P., Lopez S., 2009, *A&A*, 503, 765
 Oke J. B., Gunn J. E., 1983, *ApJ*, 266, 713
 Pascual S., Gallego J., Aragón-Salamanca A., Zamorano J., 2001, *A&A*, 379, 798
 Pérez-González P. G., Zamorano J., Gallego J., Aragón-Salamanca A., Gil de Paz A., 2003, *ApJ*, 591, 827
 Polletta M., et al., 2007, *ApJ*, 663, 81
 Rieke G. H., Alonso-Herrero A., Weiner B. J., Pérez-González P. G., Blaylock M., Donley J. L., Marcillac D., 2009, *ApJ*, 692, 556
 Salpeter E. E., 1955, *ApJ*, 121, 161
 Sanders D. B., et al., 2007, *ApJS*, 172, 86
 Scarlata C., et al., 2007, *ApJS*, 172, 406
 Schinnerer E., et al., 2004, *AJ*, 128, 1974
 Schinnerer E., et al., 2007, *ApJS*, 172, 46
 Schmidt M., 1959, *ApJ*, 129, 243
 Schmitt H. R., Calzetti D., Armus L., Giavalisco M., Heckman T. M., Kennicutt R. C., Leitherer C., Meurer G. R., 2006, *ApJ*, 643, 173

- Scoville N., et al., 2007a, ApJS, 172, 1
Scoville N., et al., 2007b, ApJS, 172, 38
Simpson C., et al., 2006, MNRAS, 372, 741
Sobral D., et al., 2009a, MNRAS, 398, 75
Sobral D., et al., 2009b, MNRAS, 398, L68
Solórzano-Iñarrea C., Best P. N., Röttgering H. J. A., Cimatti A.,
2004, MNRAS, 351, 997
Srianand R., Gupta N., Petitjean P., Noterdaeme P., Saika D. J.,
2008, MNRAS, 391, L69
Stern D., et al., 2005, ApJ, 631, 163
Sullivan M., Mobasher B., Chan B., Cram L., Ellis R., Treyer M.,
Hopkins A., 2001, ApJ, 558, 72
Tresse L., et al., 2007, A&A, 472, 403
Ueda Y., et al., 2008, ApJS, 179, 124
Villar V., Gallego J., Pérez-González P. G., Pascual S., Noeske K.,
Koo D. C., Barro G., Zamorano J., 2008, ApJ, 677, 169
Wang B., Heckman T. M., 1996, ApJ, 457, 645
Warren S. J., et al., 2007, MNRAS, 375, 213